12^{th} International Conference on Fracture Mechanics of Concrete and Concrete Structures
FraMCoS-12
B.L.A. Pichler, Ch. Hellmich, P. Preinstorfer (Eds)

https://doi.org/10.21012/FC12.1179
MS18-3:2

MULTI-SCALE MODELING OF FIBER-REINFORCED CONCRETE STRUCTURES

POURIYA PIRMORADI*, AKKE S.J. SUIKER* AND PAYAM POORSOLHJOUY*

* Department of the Built Environment, Eindhoven University of Technology,
5612 AZ Eindhoven, Netherlands
e-mail: p.pirmoradi@tue.nl

Key words: Fiber-Reinforced Concrete, Fiber Orientation, Multi-Scale Modeling, Homogenization, Granular Micromechanics Approach

Abstract. A computationally-efficient multi-scale model is developed for the analysis of fiber-reinforced concrete (FRC) structures. At the macro-scale, the structural behaviour under mechanical loading is analysed using the Finite Element Method, where in each integration point the effective constitutive response of the FRC is computed considering a representative collection of cohesive particles, fibers and air voids and applying a homogenization technique known as the Granular Micromechanics Approach. The micro-scale kinematic measures are calculated from the strain tensor in the material point by adopting the kinematic hypothesis. The micro-scale constitutive responses of the particle contacts and fibers are specified through path-dependent elasto-damage formulations. The constitutive laws of the particle contacts account for a strain-softening behavior for inter-granular tension and shear, and a strain-hardening behavior for inter-granular compression. The constitutive law for the fibers mimics the effect of elastic bonding between fiber and matrix, followed by fiber debonding and sliding under an increasing tensile load, eventually leading to complete pull-out. Under compression, the constitutive behaviour of fibers is determined by an initial, elastic branch, which continues into a failure branch that captures their combined buckling and crushing behaviour. The distribution of the fiber orientations is defined via a probability density function, and the homogenized Cauchy stress in a macro-scale material point is calculated by applying the Hill-Mandel micro-heterogeneity condition. The numerical solution procedure is strain-driven, where the macroscopic stress and tangential stiffness tensors are incrementally updated from the homogenized elasto-damage behavior of the particle contacts and fibers. The accuracy and efficiency of the multi-scale model are demonstrated by performing FEM simulations on the failure behavior of FRC samples subjected to uniaxial tensile load, and comparing the results to experimental data reported in the literature.

1 INTRODUCTION

Plain concrete is a brittle material characterized by low tensile strength and toughness, and therefore is prone to tensile fracturing that eventually may lead to catastrophic failure. A common method to improve the mechanical properties of concrete is by adding short high-strength fibers to the mix design. Since the presence of fibers restricts the propagation of cracks, fiber-reinforced concrete exhibits enhanced tensile strength, deformation capacity, and toughness in comparison with plain concrete [1].

The failure and deformation mechanisms responsible for the macro-scale constitutive behaviour of fiber-reinforced concrete involve phenomena that originate from the micro-structural level. During loading, the fiber-reinforced concrete at the micro-scale may ex-

perience tensile cracking, shear cracking and material compaction/crushing in the cementitious matrix, debonding between matrix and fiber under tensile loading, followed by fiber sliding and eventually complete fiber pull-out, and fiber micro-buckling and fiber crushing under compressive loading. Combinations of these micro-structural phenomena have been simulated with discrete lattice models, where the matrix material within the micro-structural domain is discretized by means of lattice of nodes, across which the individual fibers are randomly oriented in accordance with their fiber volume faction [2]. In addition to discrete lattice models, the micro-structural behaviour of fiber-reinforced concrete can be simulated with continuum modelling approaches, where the matrix material can be discretized by solid elements equipped with a regularized damage model and the fibers can be modelled by beam elements or truss elements with their slipping and debonding behaviour described by a fiber-matrix contact model. The spatial discretizations of the matrix material and fibers can be performed by applying conforming meshes [3], or non-conforming meshes [4].

Although the above discrete and continuum models describe the failure behaviour of fiber-reinforced composites in a meticulous fashion, their applicability for the analysis of engineering structures with a large number of fibers is limited due to the large computational demand associated with solving related boundary value problems. To circumvent this problem, efficient micro-mechanical models have been developed for the constitutive behaviour of fiber-reinforced concrete, which are based on homogenizing the micro-structural behaviour of the fibers and the matrix material across cracking planes with varying orientation characteristics, see [5] for the uniaxial tensile behaviour and [6] for the behaviour under multi-axial loading conditions. The challenges faced by these models, however, are related to solving numerical robustness problems in the FEM analyses and also defining continuum (stress and strain) measures at the cracking planes, which tend to loose their physical significance for fiber-reinforced concrete characterized by micro-structural constituents of a discrete nature [6].

In order to improve these aspects, a computationally efficient multi-scale constitutive model is developed for fiber-reinforced concrete using a homogenization method called the Granular Micromechanics Approach (GMA). In this approach, the effective constitutive response of the fiber-reinforced concrete material is calculated by homogenizing the micro-scale behaviour of its three constituents - fibers, cohesive particles and air voids - across a representative volume element. Specifically, GMA efficiently incorporates information from the micro-scale constituents into the continuum model by connecting the micro-scale properties to a probability density function describing their directional distribution, thereby avoiding the explicit modelling of the micro-structural geometry. Over the past 35 years, GMA has been successfully applied for the modelling of unreinforced granular materials characterized by various types of constitutive behaviour, see [7–10]. In the present modelling framework, the micro-scale particle contact model characterizing the cementitious matrix material is enhanced to accurately describe the concrete matrix behaviour and the model is complemented with a fiber model that accounts for the debonding, slipping and buckling/crushing behaviour of the reinforcing fibers. The two models are consistently incorporated in a GMA homogenization scheme to compute the effective, macro-scale response of the fiber-reinforced concrete. Using an incremental-iterative update algorithm, the hierarchical multi-scale constitutive model is implemented within an Finite Element Method (FEM) framework. The significance of the results is demonstrated through a comparison with experimental data reported in the literature.

2 MULTI-SCALE METHOD

2.1 Homogenization formulation

Consider a representative volume element (RVE) in the fiber-reinforced concrete material,

which is composed of its three micro-scale constituents, i.e., the cohesive particles, fibers and air voids. Consider now two neighboring particles q and p within the RVE. Adopting a Cartesian coordinate system and denoting the displacement in an arbitrary material point of the three-dimensional RVE as $\boldsymbol{u} = \{u_x, u_y, u_z\}$, the displacement components u_i^q of particle q, with $i \in \{x, y, z\}$, can be expressed as a first-order Taylor approximation of the displacement field evaluated at the neighboring particle p as

$$u_i^q \approx u_i^p + u_{i,j}^p \left(x_j^q - x_j^p\right), \tag{1}$$

where $u_{i,j}$ represents the spatial derivative of u_i in the $j-$th direction. Throughout the paper, summation convention over repeated indices is implied, unless stated otherwise. For an individual, straight fiber within the RVE, with the fiber ends m and n, the displacement components u_i^n of fiber end n can be expressed as a first-order Taylor approximation of the displacement field evaluated at the opposite fiber end m as

$$u_i^n \approx u_i^m + u_{i,j}^m \left(x_j^n - x_j^m\right). \tag{2}$$

In Eq.(1) and (2), the vectors $\boldsymbol{x}^q$ and $\boldsymbol{x}^p$ designate the centroid locations of the neighboring particles q and p, while the vectors $\boldsymbol{x}^m$ and $\boldsymbol{x}^n$ indicate the locations of the fiber ends m and n. In order to discard the effects of rigid body rotations originating from the anti-symmetric part of the displacement gradients, the displacement gradients in Eqs.(1) and (2) are replaced by their symmetric part, i.e., the strain ϵ_{ij}^p and ϵ_{ij}^m. Following the so-called kinematic hypothesis, the micro-scale strains ϵ_{ij}^p and ϵ_{ij}^m in are replaced by the average strain across the RVE, i.e., the macroscopic strain ϵ_{ij}, which turns Eqs.(1) and (2) into

$$\begin{aligned} \delta_i^\alpha &= \epsilon_{ij} l_j^\alpha \quad \text{where} \quad \alpha \in \{1, 2, ..., N_\text{c}\}, \\ \delta_i^\beta &= \epsilon_{ij} l_j^\beta \quad \text{where} \quad \beta \in \{1, 2, ..., N_\text{f}\}, \end{aligned} \tag{3}$$

where δ_i^α represents the effective relative displacement at particle contact α (i.e. the contact between two neighboring particles p and q) while δ_i^β represents the effective relative displacement between the two ends m and n of a specific fiber β. The total number of cohesive particle contacts and fibers within the RVE are represented by N_c and N_f, respectively. Further, $l_j^\alpha = x_j^q - x_j^p$ and $l_j^\beta = x_j^n - x_j^m$ denote the components of the branch vectors connecting the centroids of particles p and q and the locations of the fiber ends m and n, respectively.

The coupling between the micro-scale and macro-scale behaviour is established through the application of the Hill-Mandel micro-heterogeneity condition [15], which states that the volume average of the variational work applied at the boundaries of the RVE is equal to the local variational work per unit volume at the macro-scale. Accordingly, for an RVE with volume V that contains N_c cohesive particle contacts and N_f fibers, the variation of the macroscopic work per unit volume δW reads

$$\delta W = \frac{1}{V} \left(\sum_{\alpha=1}^{N_\text{c}} \delta W^\alpha + \sum_{\beta=1}^{N_\text{f}} \delta W^\beta \right), \tag{4}$$

where δW^α and δW^β are the variational work contributions of particle contact α and fiber β, respectively. With Eq.(3), these variational work contributions can be formulated as

$$\delta W^\gamma = f_i^\gamma l_j^\gamma \delta \epsilon_{ij} \quad \text{where} \quad \gamma : \alpha, \beta, \tag{5}$$

with f_i^α and f_i^β the components of the force vectors at particle contact α and fiber β, respectively. Here and in the following, the superscript γ refers to α for the a cohesive contact and β for a specific fiber. In order to further elaborate Eq.(4), at each particle contact α and fiber β a local Cartesian coordinate system is introduced that is defined by the three orthonormal base vectors, $\mathbf{n}^\gamma$, $\mathbf{s}^\gamma$, and $\mathbf{t}^\gamma$. Here, $\mathbf{n}^\gamma$ is the unit vector in the normal/axial direction of the particle contact/fiber, and $\mathbf{s}^\gamma$ and $\mathbf{t}^\gamma$ are the unit vectors in the two (mutually perpendicular) tangential/transversal directions of the particle contact/fiber. The right-handed orthonormal base vectors $\{\mathbf{n}^\gamma, \mathbf{s}^\gamma, \mathbf{t}^\gamma\}$ can be expressed in terms of the orthonormal base vec-

tors $\{\mathbf{i}, \mathbf{j}, \mathbf{k}\}$ of the global x-y-z coordinate system via

$$\begin{cases} \mathbf{n}^\gamma = \sin\theta^\gamma \cos\phi^\gamma \, \mathbf{i} + \sin\theta^\gamma \sin\phi^\gamma \, \mathbf{j} + \cos\theta^\gamma \, \mathbf{k} \,, \\ \mathbf{s}^\gamma = \cos\theta^\gamma \cos\phi^\gamma \, \mathbf{i} + \cos\theta^\gamma \sin\phi^\gamma \, \mathbf{j} \, - \sin\theta^\gamma \, \mathbf{k} \,, \\ \mathbf{t}^\gamma = \mathbf{n}^\gamma \times \mathbf{s}^\gamma = -\sin\phi^\gamma \, \mathbf{i} + \cos\phi^\gamma \, \mathbf{j} \,, \end{cases} \tag{6}$$

in which $\theta^\gamma \in [0, \pi]$ and $\phi^\gamma \in [0, 2\pi]$ are the polar and azimuthal angles defining the individual particle contact orientations and fiber orientations. With Eq.(6), the effective relative displacements at particle contact α and fiber β can be written in terms of the components along the axes of the local coordinate system as

$$\delta_{\mathrm{n}}^\gamma = \delta_i^\gamma n_i^\gamma, \quad \delta_{\mathrm{s}}^\gamma = \delta_i^\gamma s_i^\gamma, \quad \delta_{\mathrm{t}}^\gamma = \delta_i^\gamma t_i^\gamma. \tag{7}$$

The magnitude of the effective tangential displacement follows as $\delta_{\mathrm{w}}^\gamma = ((\delta_{\mathrm{s}}^\gamma)^2 + (\delta_{\mathrm{t}}^\gamma)^2)^{1/2}$. Here we note that the subscripts n, s, t, and w do not refer to global coordinate components and therefore *do not* follow the summation convention. The normal and tangential components of force in particle contact α and fiber β can be formally expressed as

$$f_{\mathrm{n}}^\gamma = \hat{f}_{\mathrm{n}}^\gamma(\delta_{\mathrm{n}}^\gamma, \delta_{\mathrm{w}}^\gamma), \quad \text{and} \quad f_{\mathrm{w}}^\gamma = \hat{f}_{\mathrm{w}}^\gamma(\delta_{\mathrm{n}}^\gamma, \delta_{\mathrm{w}}^\gamma), \tag{8}$$

with the superimposed hat denoting a functional dependency of the contact force. The effective tangential/transverse force f_{w}^γ can be straightforwardly decomposed along the two local tangential/transverse directions $\mathbf{s}^\gamma$ and $\mathbf{t}^\gamma$, and accordingly the force vectors at particle contact α and fiber β may be expressed in the global x-y-z coordinate system via

$$f_i^\gamma = f_{\mathrm{n}}^\gamma n_i^\gamma + f_{\mathrm{s}}^\gamma s_i^\gamma + f_{\mathrm{t}}^\gamma t_i^\gamma. \tag{9}$$

As a next step, the macroscopic variational work per unit volume δW appearing in the left-hand side of Eq.(4) is developed as

$$\delta W = \frac{\partial W}{\partial \epsilon_{ij}} \delta\epsilon_{ij} = \sigma_{ij} \, \delta\epsilon_{ij}, \tag{10}$$

where σ_{ij} represents the components of the macroscopic Cauchy stress tensor. Substituting Eqs.(5) and (10) into the Hill-Mandel condition, Eq.(4), and considering that the condition should hold for any arbitrary strain variations $\delta\epsilon_{ij}$, the effective, homogenized Cauchy stress across the RVE can be expressed as

$$\sigma_{ij} = \frac{1}{V} \left(\sum_{\alpha=1}^{N_{\mathrm{c}}} f_i^\alpha l_j^\alpha + \sum_{\beta=1}^{N_{\mathrm{f}}} f_i^\beta l_j^\beta \right). \tag{11}$$

In Eq.(11), the macroscopic stress is computed for an RVE containing a finite number of cohesive particle contacts and fibers, namely N_{c} and N_{f}. For an RVE with sufficiently large number of particle contacts and fibers, Eq.(11) may be replaced by an integral expression as

$$\begin{aligned} \sigma_{ij} \;&=\; \frac{N_{\mathrm{c}}}{V} \int_{\phi=0}^{2\pi} \int_{\theta=0}^{\pi} f_i^\alpha \, l_j^\alpha \, \xi^\alpha \sin\theta \, \mathrm{d}\theta \, \mathrm{d}\phi \\ &+\; \frac{N_{\mathrm{f}}}{V} \int_{\phi=0}^{2\pi} \int_{\theta=0}^{\pi} f_i^\beta \, l_j^\beta \, \xi^\beta \sin\theta \, \mathrm{d}\theta \, \mathrm{d}\phi \,, \end{aligned} \tag{12}$$

where ξ^γ is the probability density function that represents the directional distribution of the particle contact and fiber properties [10].

The expression for the macroscopic stress given by Eq.(12) can be further elaborated by assuming that the fiber-reinforced concrete consists of equal-sized spherical particles with radius r and equal-sized cylindrical fibers with cross-sectional radius R and length L. Accordingly, the number of cohesive particle contacts per unit volume, N_{c}/V, and the number of fibers per unit volume, N_{f}/V, can be expressed as

$$\frac{N_{\mathrm{c}}}{V} = \frac{3\bar{n} v_{\mathrm{m}}}{8\pi r^3} \quad \text{and} \quad \frac{N_{\mathrm{f}}}{V} = \frac{v_{\mathrm{f}}}{\pi R^2 L}, \tag{13}$$

where $\bar{n} = 2N_c/N_p$ is co-ordination number representing the average number of contacts per particle, v_{f} is the volume fraction of fibers, and v_{m} is the volume fraction of matrix. The macroscale Cauchy stress then becomes

$$\begin{aligned} \sigma_{ij} \;&=\; \frac{3\bar{n} v_{\mathrm{m}}}{4\pi r^2} \int_{\phi=0}^{2\pi} \int_{\theta=0}^{\pi} f_i^\alpha \, n_j \, \xi^\alpha \sin\theta \, \mathrm{d}\theta \, \mathrm{d}\phi \\ &+\; \frac{v_{\mathrm{f}}}{\pi R^2} \int_{\phi=0}^{2\pi} \int_{\theta=0}^{\pi} f_i^\beta \, n_j \, \xi^\beta \sin\theta \, \mathrm{d}\theta \, \mathrm{d}\phi \,. \end{aligned} \tag{14}$$

The micro-scale forces $\mathbf{f}^{\alpha}$ and $\mathbf{f}^{\beta}$ in the above equation are prescribed by specific micro-scale constitutive relations, which are presented in Section 2.2 below.

2.2 Micro-scale constitutive relations

Upon the application of mechanical loading, the fiber-reinforced concrete at the micro-scale may experience various damage effects which are accounted for in the model by expressing the micro-scale force-displacement relations, Eq.(8), through a damage formulation. Under *tensile loading* the constitutive relation in the normal/axial direction of a cohesive particle contact α and fiber β is given by

$$f_{\mathrm{n}}^{\gamma} = (1 - D_{\mathrm{n,t}}^{\gamma}) K_{\mathrm{n,t}}^{\gamma} \delta_{\mathrm{n}}^{\gamma}, \quad \text{if} \quad \delta_{\mathrm{n}}^{\gamma} \geq 0, \tag{15}$$

while under *compressive loading* it reads

$$f_{\mathrm{n}}^{\gamma} = (1 - D_{\mathrm{n,c}}^{\gamma}) K_{\mathrm{n,c}}^{\gamma} \delta_{\mathrm{n}}^{\gamma}, \quad \text{if} \quad \delta_{\mathrm{n}}^{\gamma} < 0. \tag{16}$$

Further, under *shear loading* the constitutive relation in the tangential/transversal direction of a cohesive particle contact α and fiber β reads

$$f_{\mathrm{w}}^{\gamma} = (1 - D_{\mathrm{w}}^{\gamma}) K_{\mathrm{w}}^{\gamma} \delta_{\mathrm{w}}^{\gamma}. \tag{17}$$

In Eqs.(15) to (17), $K_{\mathrm{n,t}}^{\gamma}$, $K_{\mathrm{n,c}}^{\gamma}$, and K_{w}^{γ} are the initial tensile, compressive, and shear stiffness coefficients, respectively. Further, $D_{\mathrm{n,t}}^{\gamma}$, $D_{\mathrm{n,c}}^{\gamma}$, and D_{w}^{γ} are the tensile, compressive and shear damage variables, respectively, which are expressed as functions of deformation history variables as

$$D_{\mathrm{n,t}}^{\gamma} = \hat{D}_{\mathrm{n,t}}^{\gamma}(\kappa_{\mathrm{t}}^{\gamma}, \kappa_{\mathrm{w}}^{\gamma}), \quad D_{\mathrm{n,c}}^{\gamma} = \hat{D}_{\mathrm{n,c}}^{\gamma}(\kappa_{\mathrm{c}}^{\gamma}, \kappa_{\mathrm{w}}^{\gamma}),$$
$$D_{\mathrm{w}}^{\gamma} = \begin{cases} \hat{D}_{\mathrm{w}}^{\gamma}(\kappa_{\mathrm{t}}^{\gamma}, \kappa_{\mathrm{w}}^{\gamma}) & \text{if} \quad \delta_{\mathrm{n}}^{\gamma} \geq 0 \\ \hat{D}_{\mathrm{w}}^{\gamma}(\kappa_{\mathrm{c}}^{\gamma}, \kappa_{\mathrm{w}}^{\gamma}) & \text{if} \quad \delta_{\mathrm{n}}^{\gamma} < 0 \end{cases}, \tag{18}$$

where $\kappa_{\mathrm{t}}^{\gamma}$, $\kappa_{\mathrm{c}}^{\gamma}$, and $\kappa_{\mathrm{w}}^{\gamma}$ are the deformation history variables under tension, compression, and shear, representing the maximum displacement experienced during the loading history. The damage variables may vary between zero and one, where the initial, zero value corresponds to the undamaged, elastic state of the micro-scale constituent, and the value of one reflects the state at which the constituent fails by a complete loss of strength and/or an unlimited growth of deformation.

For modeling the *quasi-brittle cracking* response under *tensile* loading in Eq.(15), the tensile damage variable and the initial tensile stiffness of particle contact α are specified as

$$D_{\mathrm{n,t}}^{\alpha} = 1 - \exp(-\frac{\kappa_{\mathrm{t}}^{\alpha}}{B_{\mathrm{t}}^{\alpha}}) \ \text{ and } \ K_{\mathrm{n,t}}^{\alpha} = A, \tag{19}$$

where A denotes the initial tensile stiffness and B_{t}^{α} reflects the normal contact displacement at which the ultimate tensile strength is reached. To account for the reduction in the tensile contact force due to damage development under shear loading, the parameter B_{t}^{α} is assumed to linearly reduce with increasing shear displacement history variable $\kappa_{\mathrm{w}}^{\alpha}$ in accordance with Figure 1(b).

For simulating *material compaction/crushing* under *compressive* loading, the compressive damage parameter and the elastic compressive stiffness of particle contact α are formulated as

$$D_{\mathrm{n,c}}^{\alpha} = 1 - M\frac{\arctan(A\kappa_{\mathrm{c}}^{\alpha}/M)}{A\kappa_{\mathrm{c}}^{\alpha}} \ \text{ and } \ K_{\mathrm{n,c}}^{\alpha} = A, \tag{20}$$

with A the initial compressive stiffness and M a parameter that governs the contact's compressive strength. To account for the strengthening effect caused by the macroscopic compressive hydrostatic stress, $P = -\min(\sigma_{ii}/3, 0)$, on the cohesive contact, the parameter M is defined as

$$M = M_0 \left(1 + \alpha_1 \left(\frac{P}{P_{\mathrm{ref}}}\right)^{\alpha_2}\right), \tag{21}$$

where M_0 represents the initial value at $P = 0$, α_1 and α_2 are calibration factors, and P_{ref} is a reference pressure taken as $P_{\mathrm{ref}} = 1$ MPa.

Finally, for modeling the *quasi-brittle cracking* response under *shear* loading, the damage variable and the elastic stiffness in the tangential direction of the particle contact α follows

$$D_{\mathrm{w}}^{\alpha} = 1 - \exp(-\frac{\kappa_{\mathrm{w}}^{\alpha}}{B_{\mathrm{w}}^{\alpha}}) \ \text{ and } \ K_{\mathrm{w}}^{\alpha} = C, \tag{22}$$

where C is the initial shear stiffness and B_{w}^{α} is the tangential contact displacement at which the

ultimate shear strength is reached. To account for the reduction in the shear contact force due to damage development under tension, the parameter B_{w}^{α} is assumed to linearly reduce with increasing tensile displacement history variable $\kappa_{\mathrm{t}}^{\alpha}$ in accordance with Figure 1(f). Conversely, under compressive loading the parameter B_{w}^{α} is constant, $B_{\mathrm{w}}^{\alpha} = \alpha_3 B_{\mathrm{w0}}$, with α_3 a calibration parameter. The micro-scale constitutive relationships for cohesive contacts, including the behavior during loading, unloading, and reloading are summarized in Figure 1

At the micro-scale, the contribution of fibers to the overall mechanical performance of the fiber-reinforced concrete may be essentially attributed to their behaviour in axial direction. Assuming the fiber tensile strength to be sufficiently high to prevent fiber rupture, their behavior can be characterized by following three phases: i) elastic bonding, ii) debonding, and iii) frictional sliding, eventually leading to complete fiber pull-out. During the bonding phase, the fiber adheres to the surrounding, intact elastic matrix and the axial force in the fiber increases linearly with the relative axial displacement between the fiber ends. After tensile cracking develops in the surrounding matrix, the relative axial displacement $\delta_{\mathrm{n}}^{\beta}$ attains a value d_{b} corresponding to the elastic bonding limit, $f_{\mathrm{n}}^{\beta} = f_{\mathrm{b}}$, at which the fiber starts to debond from the matrix through the development of a delamination crack. The mechanical resistance of the fiber against deformation then reduces, and is determined by a combination of interfacial decohesion and frictional sliding along the debonded zone and elastic bonding along the intact parts. Once the delaminating crack has reached the ends of the fiber, the fiber becomes fully debonded from the matrix, which occurs when the relative axial displacement is $\delta_{\mathrm{n}}^{\beta} = d_{\mathrm{d}}$ and the axial fiber force has reached the value $f_{\mathrm{n}}^{\beta} = f_{\mathrm{d}}$. The fiber is then gradually pulled out of the matrix and its mechanical resistance is entirely controlled by the frictional sliding mobilized along the actual contact area with the matrix. The axial force f_{n}^{β} monotonically decreases as the frictional contact area between fiber and matrix reduces and eventually vanishes at complete fiber pull-out, which occurs when the the relative axial displacement reaches $\delta_{n}^{\beta} = d_{\mathrm{s}}$. Figure 2(a) demonstrates the idealized fiber *tensile failure response* discussed above, along with the elastic unloading and reloading branches. The three distinct response phases under tensile loading can be modeled with the damage formulation Eq.(15), by expressing the tensile damage variable and the elastic tensile stiffness in the axial direction of fiber β as

$$D_{\mathrm{n,t}}^{\beta} = \begin{cases} 0 & \text{if } \ 0 \leq \kappa_{\mathrm{t}}^{\beta} < d_{\mathrm{b}} \\ 1 - \left(\left(\dfrac{f_{\mathrm{b}} d_{\mathrm{d}} - f_{\mathrm{d}} d_{\mathrm{b}}}{f_{\mathrm{b}}(d_{\mathrm{d}} - d_{\mathrm{b}})} \right) \dfrac{d_{\mathrm{b}}}{\kappa_{\mathrm{t}}^{\beta}} + \left(\dfrac{(f_{\mathrm{d}} - f_{\mathrm{b}}) d_{\mathrm{b}}}{f_{\mathrm{b}}(d_{\mathrm{d}} - d_{\mathrm{b}})} \right) \right) & \text{if } \ d_{\mathrm{b}} \leq \kappa_{\mathrm{t}}^{\beta} < d_{\mathrm{d}} \\ 1 - \left(\dfrac{f_{\mathrm{d}} d_{\mathrm{b}}}{f_{\mathrm{b}}(d_{\mathrm{s}} - d_{\mathrm{d}})} \right) \left(\dfrac{d_{\mathrm{s}}}{\kappa_{\mathrm{t}}^{\beta}} - 1 \right) & \text{if } \ d_{\mathrm{d}} \leq \kappa_{\mathrm{t}}^{\beta} < d_{\mathrm{s}} \\ 1 & \text{if } \ \kappa_{\mathrm{t}}^{\beta} \geq d_{\mathrm{s}} \end{cases} \quad \text{and} \quad K_{\mathrm{n,t}}^{\beta} = \frac{f_{\mathrm{b}}}{d_{\mathrm{b}}}. \tag{23}$$

The strengthening effect on the fiber tensile response caused by the macroscopic compressive hydrostatic stress P is accounted for by defining the parameters f_{b} and f_{d} as

$$\begin{cases} f_{\mathrm{b}} = f_{\mathrm{b0}} \left(1 + \alpha_4 \left(\dfrac{P}{P_{\mathrm{ref}}} \right) \right) \\ f_{\mathrm{d}} = f_{\mathrm{d0}} \left(1 + \alpha_4 \left(\dfrac{P}{P_{\mathrm{ref}}} \right) \right) \end{cases} \tag{24}$$

where f_{b0} and f_{d0} are the initial parameter values corresponding to zero compressive hydrostatic stress, and α_4 is a calibration factor.

The *compressive failure response* of individual fibers is characterized by different failure modes, including elastic microbuckling, plastic microbuckling and/or fiber crushing. For simplicity, in the present work the different failure modes are simulated by one and the same,

generic, limit load model, which is composed of an initial, elastic branch and a horizontal failure branch. The compressive damage variable in the damage model Eq.(16) is defined accordingly as

$$D_{\mathrm{n,c}}^{\beta} = \begin{cases} 0 & \text{if} \quad d_{\mathrm{c,u}} \leq \kappa_{\mathrm{c}}^{\beta} \leq 0\,, \\ 1 - \dfrac{d_{\mathrm{c,u}}}{\kappa_{\mathrm{c}}^{\beta}} & \text{if} \quad \kappa_{\mathrm{c}}^{\beta} < d_{\mathrm{c,u}}\,, \end{cases} \tag{25}$$

while the elastic compressive stiffness of a fiber reads

$$K_{\mathrm{n,c}}^{\beta} = \frac{f_{\mathrm{c,u}}}{d_{\mathrm{c,u}}}. \tag{26}$$

Here, $f_{\mathrm{c,u}}$ is the ultimate compressive strength at which the elastic response ends and the fiber collapses, and $d_{\mathrm{c,u}}$ is the corresponding relative axial displacement between the fiber ends. The microscopic constitutive relationships for fibers, including the behavior during loading, unloading, and reloading are summarized in Figure 2.

The current micro-scale constitutive model in total consists of 18 material parameters, including 9 material parameters for describing the tensile behaviour of particles and fibers, 5 material parameters for defining their compressive behaviour, and 4 material parameters for characterizing the shear behaviour of particles. For a specific mix design of the fiber-reinforced concrete, the micro-scale material parameters are determined via a calibration procedure using macroscopic test results, which are shown in Section 3.

2.3 Numerical implementation procedure

The developed hierarchical multi-scale model is implemented to analyze practical boundary value problems for fiber-reinforced concrete structures. In each macroscopic integration point (or material point) mechanical equilibrium should be satisfied under the appropriate boundary conditions, which, in the absence of body forces, reads

$$\boldsymbol{\nabla} \cdot \boldsymbol{\sigma} = \mathbf{0}\,, \tag{27}$$

with $\boldsymbol{\nabla}\cdot$ the divergence operator. Since the micro-scale material behaviour is inelastic and path-dependent, the macroscopic stress $\boldsymbol{\sigma}$ must be computed in an *incremental* fashion, by stepwisely loading the FEM domain from its initial state to the actual state of deformation. Accordingly, consider an individual macroscopic loading step, expressed in an integration point by the change in strain going from step n to step $n+1$:

$$\boldsymbol{\epsilon}_{n+1} = \boldsymbol{\epsilon}_n \, + \, \Delta\boldsymbol{\epsilon}_{n+1}\,, \tag{28}$$

with $\Delta\boldsymbol{\epsilon}_{n+1}$ the incremental strain at the current step $n+1$. From the strain update $\boldsymbol{\epsilon}_{n+1}$, the multi-scale failure model calculates the corresponding stress update $\boldsymbol{\sigma}_{n+1}$ in an integration point as follows. First, $\boldsymbol{\epsilon}_{n+1}$ is inserted in Eq.(3) to compute the displacements at the particle contacts and fibers in the global, macroscopic Cartesian coordinate system. Next, by applying Eq.(7), these displacements are converted to the local Cartesian coordinate system of each particle contact and fiber. From these displacement components, the corresponding force components at the local coordinate system are computed via the micro-scale constitutive relations, Eqs.(15) to (17). This step requires updating the tensile, compressive, and shear damage variables which follow from the updates of the corresponding history variables in accordance with the micro-scale constitutive models presented in Sections 2.2. Next, the updated force components are converted to the global coordinate systems using Eq.(9), and subsequently inserted in Eq.(14) to compute the macroscopic stress $\boldsymbol{\sigma}_{n+1}$ in the integration point. The surface integrals in Eq.(14) for computing macroscopic stress are computed numerically using Lebedev quadrature. The above procedure is performed for all integration points in the simulated FEM domain, where the updated stresses $\boldsymbol{\sigma}_{n+1}$ are transferred to the system level of the FEM simulation. In addition, the components of the consistent tangent operator are updated as $C_{ijkl} = \mathrm{d}\,\sigma_{ij}/\mathrm{d}\,\epsilon_{kl}$ using the numerical perturbation method formulated in [12]. The stress and tangent components are then transferred to the system level to compose the internal force and structural stiffness matrix in the global system of equilibrium equations. When the system

of global equilibrium equations has converged within a prescribed tolerance, the implicit update procedure is repeated for the next incremental loading step, as expressed by Eq.(28).

3 NUMERICAL RESULTS

The main characteristics of the multi-scale model presented in the previous section are demonstrated by performing simulations on the failure behaviour of fiber-reinforced concrete samples subjected to uniaxial tensile test. Figures 3 illustrates the results (solid lines) for uniaxial tension tests on concrete specimens reinforced by PVA fibers with volume fractions of $v_{\rm f} = 2\%$, 3% and 6%, and for a uniaxial tensile test on a plain concrete specimen. The results are plotted together with the experimental data (open circles) reported in [13].

In the numerical simulations, the uniaxial tensile loading is applied displacement-controlled, where the effective normal strain ϵ_1 in the axial direction is increased stepwisely, and the normal stresses are zero on the lateral sample surfaces, $\sigma_2 = \sigma_3 = 0$. The numerical results are computed using the material parameter values listed in Table 1. In addition, The values for the fiber length, L = 32 mm, fiber radius, R = 0.4 mm, and average particle radius are taken from [13]. Further, the average coordination number $\bar{n} = 8$ is chosen as a representative value for a cementitious matrix and a value of air void content $v_{\rm v} = 3\%$ is selected in the numerical simulations. In the experimental samples the aggregates and fibers are distributed randomly, so that the particle contacts and fibers follow a uniform directional distribution, $\xi^{\alpha} = \xi^{\beta} = 1/(4\pi)$. The results in Figure 3 clearly show that an increase of the fiber volume fraction leads to an increase of both the ultimate tensile strength and the ductility of the sample.

The directional distribution of fibers in fiber reinforced concrete depends on the production and construction processes, and thus under specific process conditions may be (strongly) non-uniform. For instance, in 3D printed fiber-reinforced concrete structures the fibers show an orientation preference in the printing direction caused by the extrusion processes. The effect of different fiber direction distributions on the uniaxial tensile response of fiber-reinforced concrete can be explored by varying the probability density function of fiber ξ^{β}. Accordingly, three different fiber direction distributions are considered, namely: Case (1): a uniform fiber orientation distribution, Case (2): a distribution where the fibers are predominantly oriented in the loading direction, and Case (3): a distribution where the fibers are predominantly oriented perpendicular to the loading direction. For Cases (2) and (3), the probability density function of fibers is described by a transversely isotropic distribution oriented in the corresponding direction as

$$\xi^{\beta}(\theta) = \frac{3\cos^2\theta}{4\pi}. \tag{29}$$

Figure 4 shows the uniaxial stress-strain responses computed for concrete samples reinforced by $v_{\rm f} = 3\%$ of PVA fibers, applying the three different fiber direction distributions described above. This figure demonstrates that the sample with the fibers oriented in the loading direction are characterized by the highest secant stiffness and highest ultimate tensile strength, followed by the sample with the uniform fiber orientation distribution, and finally the sample with the fibers oriented perpendicular to the loading direction. In addition, the sample with the fibers oriented in the loading direction show an almost constant maximum stress under increased deformation, while the other two samples are characterized by a softening response. These features arise from the increased contribution to the tensile response by crack-bridging fibers, and are in agreement with other experimental results [14].

4 Concluding remarks

A multi-scale constitutive model is developed for the efficient computational analysis of fiber-reinforced concrete structures. In a macro-scale material point the effective constitutive response of the fiber-reinforced concrete material is calculated by homogenizing the micro-scale

behaviour of its three constituents – fibers, cohesive particles and air voids – across a representative volume element. The constitutive contact law for the cohesive particles accounts for the fracture behaviour under intergranular tension and shear, and the compaction/crushing behaviour under intergranular compression. For the fibers, the tensile constitutive law is characterized by an initial elastic bonding between fiber and matrix, followed by fiber debonding and sliding and eventually complete pull-out. Under compression, the constitutive behaviour of fibers is determined by an initial, elastic branch, which continues into a failure branch that captures their combined buckling and crushing behaviour. The orientation distributions of the particle contacts and fibers are defined by separate probability density functions, and the effective Cauchy stress in a macro-scale material point is calculated by applying the Hill-Mandel micro-heterogeneity condition. Using an incremental-iterative update algorithm, the hierarchical multi-scale constitutive model is implemented within a Finite Element Method (FEM) framework. The applicability of the multi-scale model is exemplified by performing simulations of fiber-reinforced concrete samples under uniaxial tension tests. The numerical results illustrate how the structural response is influenced by the changes in the volume fraction and orientation distribution of fibers. The significance of the results is demonstrated through a comparison with experimental data reported in the literature.

The present model enables the efficient numerical simulation of practical boundary value problems, where, for a fiber-reinforced material with given constitutive properties, it allows to adequately predict the effects of fibers content, fiber orientation distribution, loading and boundary conditions, and structural geometry on the mechanical response. In this way, the multi-scale model may be utilized as an engineering tool for the practical analysis of the complex failure behaviour of fiber-reinforced concrete structures.

REFERENCES

[1] Li, V. C., *Engineered cementitious composites (ECC): bendable concrete for sustainable and resilient infrastructure*, Springer, 2019.

[2] Schauffert, E. A. Cusatis, G. 2012. Lattice discrete particle model for fiber-reinforced concrete. I: Theory. *Journal of Engineering Mechanics* **138**:826–833.

[3] Zhang, H. Huang, Y. J. Yang, Z. J. Xu, S. L. Chen, X. W. 2018. A discrete-continuum coupled finite element modelling approach for fibre reinforced concrete. *Cement and Concrete Research* **106**:130–143.

[4] Bitencourt, L. A. G. Manzoli, O. L. Bittencourt, T. N. Vecchio, F. J. 2019. Numerical modeling of steel fiber reinforced concrete with a discrete and explicit representation of steel fibers. *International Journal of Solids and Structures* **159**:171–190.

[5] Yang, E. H. Wang, S. Yang, Y. Li, V. C. 2008. Fiber-bridging constitutive law of engineered cementitious composites. *Journal of Advanced Concrete Technology* **6**:181–193.

[6] Caner, F. C. Bažant, Z. P. Wendner, R. 2013. Microplane model M7f for fiber reinforced concrete. *Engineering Fracture Mechanics* **105**:41–57.

[7] Suiker, A. S. J. Chang, C. S. 2004. Modeling failure and deformation of an assembly of spheres with frictional contacts. *Journal of Engineering Mechanics* **130**:283–293.

[8] Poorsolhjouy, P. Misra, A. 2017. Effect of intermediate principal stress and loading-path on failure of cementitious materials using granular micromechanics. *International Journal of Solids and Structures* **108**:139–152.

[9] Misra, A. Poorsolhjouy, P. 2020. Granular micromechanics model for damage and plasticity of cementitious materials based upon thermomechanics. *Mathematics and Mechanics of Solids* **25**:1778–1803.

[10] Pirmoradi, P. Suiker, A. S. J. Poorsolhjouy, P. 2024. Anisotropic elastic strain-gradient continuum from the macro-scale to the granular micro-scale. *Journal of Elasticity* **156**:647–680.

[11] Lebedev, V. I. Laikov, V. N. 1999. A quadrature formula for the sphere of the 131st algebraic order of accuracy. *Russian Academy of Sciences Doklady Mathematics* **59**:477–481.

[12] Suiker, A. S. J. Turteltaub, S. A. 2005. Computational modelling of plasticity induced by martensitic phase transformations. *International Journal for Numerical Methods in Engineering* **63**:1655–1693.

[13] Li, Z. Li, F. Chang, T. Y. P. Mai, Y. W. 1999. Uniaxial tensile behavior of concrete reinforced with randomly distributed short fibers. *Materials Journal* **95**:564–574.

[14] Abrishambaf, A. Pimentel, M. Nunes, S. 2017. Influence of fibre orientation on the tensile behaviour of ultra-high performance fibre reinforced cementitious composites. *Cement and Concrete Research* **97**:28–40.

[15] Hill, R. 1963. Elastic properties of reinforced solids: some theoretical principles. *Journal of the Mechanics and Physics of Solids* **111**:357–372.

Particle contacts		PVA fibers			
A [N/mm]	1.35×10^5	v_{f} [%]	2	3	6
B_0 [mm]	2.62×10^{-4}	f_{b0} [N]	20.4	20.4	13.2
$\kappa_{\mathrm{w,cr}}$ [mm]	7.82×10^{-3}	d_{b} [mm]	7.86×10^{-4}	7.86×10^{-4}	7.86×10^{-4}
M_0 [N]	-124.3	f_{d0} [N]	102.0	102.0	65.7
α_1 [-]	0.296	d_{d} [mm]	1.57×10^{-2}	1.57×10^{-2}	1.57×10^{-2}
α_2 [-]	1	d_{s} [mm]	7.86×10^{-1}	7.86×10^{-1}	7.86×10^{-1}
C [N/mm]	8.11×10^4	$f_{\mathrm{c,u}}$ [N]	-102.0	-102.0	-102.0
B_{w0} [mm]	5.24×10^{-4}	$d_{\mathrm{c,u}}$ [mm]	-3.93×10^{-3}	-3.93×10^{-3}	-3.93×10^{-3}
$\kappa_{\mathrm{t,cr}}$ [mm]	3.91×10^{-3}	α_4 [-]	2.96×10^{-2}	2.96×10^{-2}	2.96×10^{-2}
α_3 [-]	4				

Table 1: Micro-scale material parameters for the particle contacts defining the cementitious matrix and the PVA fibers

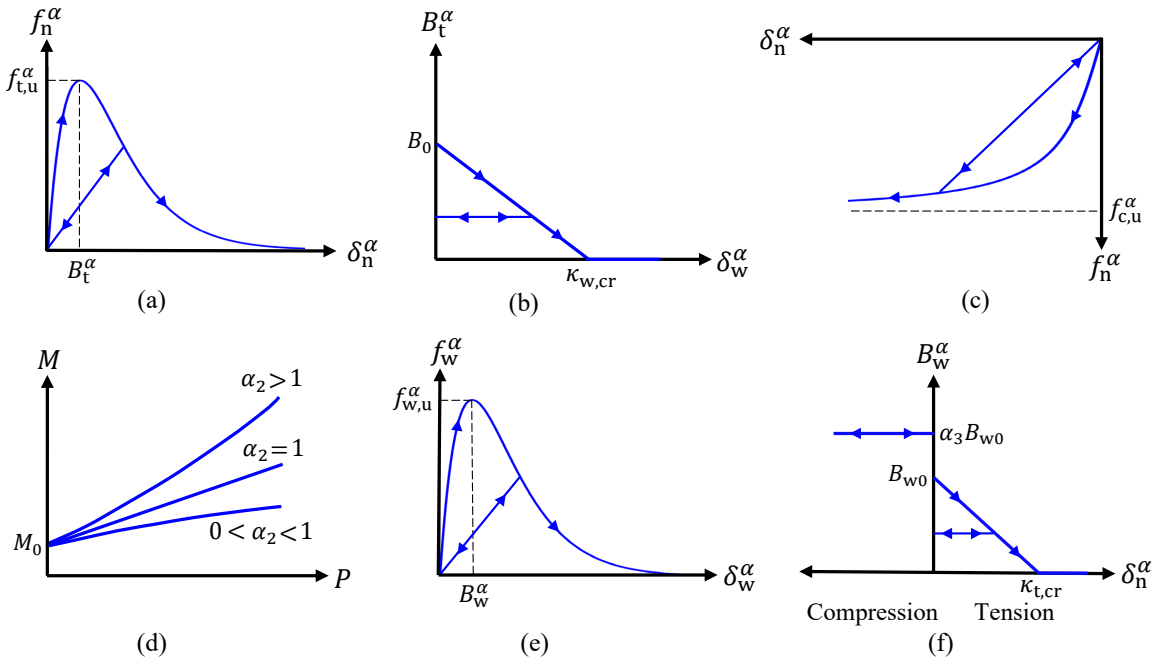

Figure 1: Micro-scale constitutive relationships at particle contact α. (a) Tensile contact force f_n^α versus normal contact displacement δ_n^α. (b) Tensile contact parameter B_t^α versus tangential contact displacement δ_w^α. (c) Compressive contact force f_n^α versus normal contact displacement δ_n^α. (d) Compressive strengthening parameter M versus hydrostatic pressure P. (e) Shear contact force f_w^α versus tangential contact displacement δ_w^α. (f) Shear contact parameter B_w^α versus normal contact displacement δ_n^α.

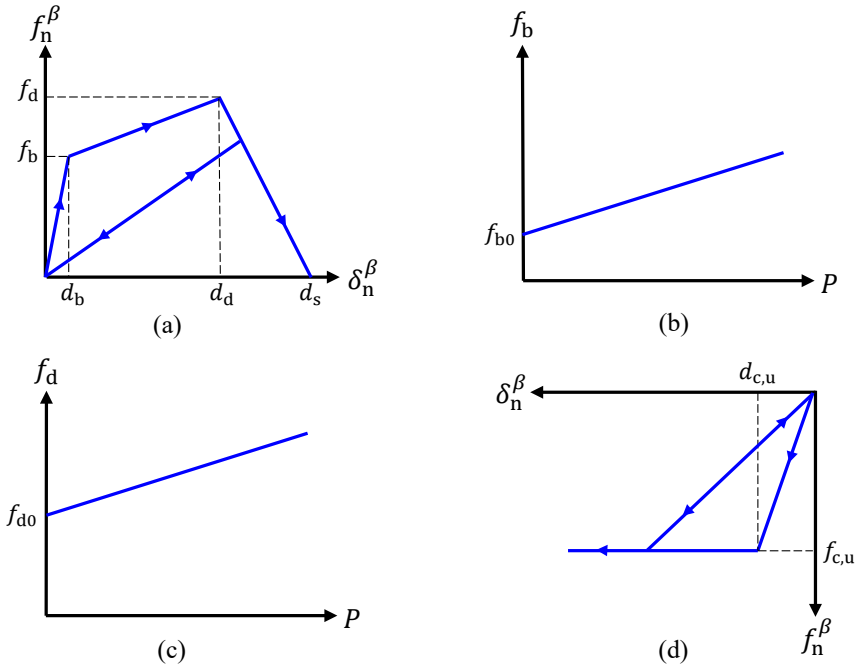

Figure 2: Micro-scale constitutive relationships of fiber β. (a) Tensile fiber force f_n^β versus relative axial displacement δ_n^β. (b) Elastic bonding limit f_b versus hydrostatic pressure P. (c) Debonding limit f_d versus hydrostatic pressure P. (d) Compressive fiber force f_n^β versus relative axial displacement δ_n^β.

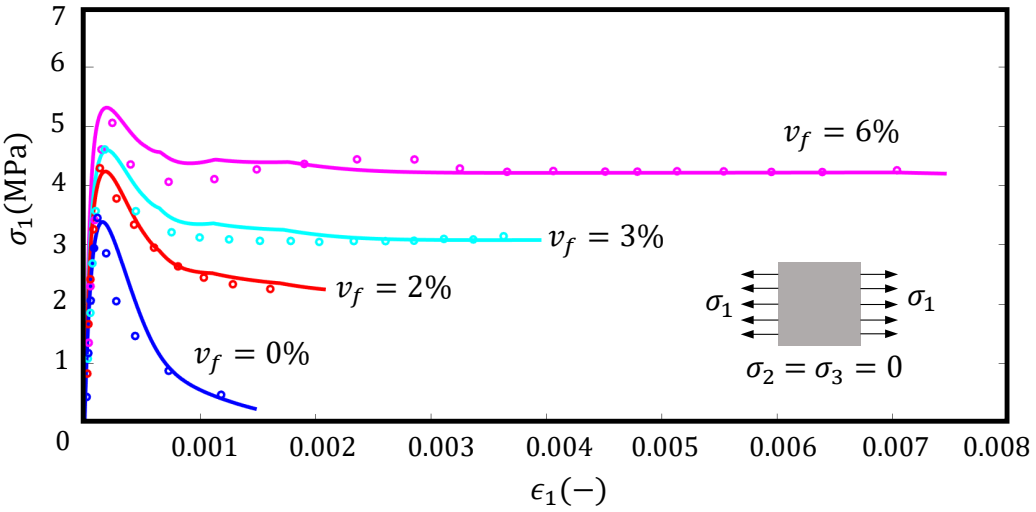

Figure 3: FEM results (solid lines) and experimental data (open circles) [13] for the uniaxial tensile response of concrete specimens reinforced by PVA fibers with a uniform fiber orientation distribution. The fiber volume fractions are equal to $v_{\mathrm{f}} = 2\%$, 3% and 6%. Additionally, the response for a uniaxial tensile test on a plain concrete specimen, $v_{\mathrm{f}} = 0\%$, is depicted.

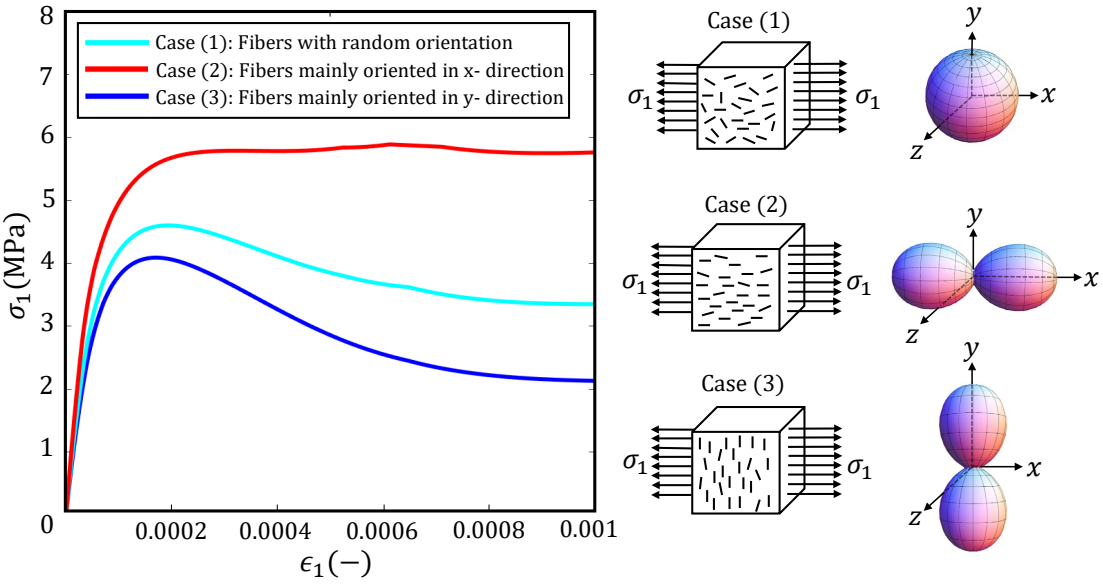

Figure 4: FEM results for the uniaxial tensile response of concrete specimens reinforced by PVA fibers ($v_{\mathrm{f}} = 3\%$) with three different directional distributions (as indicated in the right image), i.e., Case (1): a uniform fiber orientation distribution, Case (2): a distribution where the fibers are predominantly oriented in the loading direction, and Case (3): a distribution where the fibers are predominantly oriented perpendicular to the loading direction.